Flexible Microfluidic Fabrication of Oil-Encapsulated Alginate Microfibers

A.S. Chaurasia, F. Jahanzad, S. Sajjadi

PII: S1385-8947(16)31290-6
DOI: http://dx.doi.org/10.1016/j.cej.2016.09.054
Reference: CEJ 15764

To appear in: *Chemical Engineering Journal*

Received Date: 6 June 2016
Revised Date: 4 September 2016
Accepted Date: 12 September 2016

Please cite this article as: A.S. Chaurasia, F. Jahanzad, S. Sajjadi, Flexible Microfluidic Fabrication of Oil-Encapsulated Alginate Microfibers, *Chemical Engineering Journal* (2016), doi: http://dx.doi.org/10.1016/j.cej.2016.09.054

Flexible Microfluidic Fabrication of Oil-Encapsulated Alginate Microfibers

A. S. Chaurasia,[a] F. Jahanzad[b] and S. Sajjadi[a†]

[a] *Department of Physics, King's College London, Strand, London, WC2R 2LS, UK*

[b] *Division of Chemical and Petroleum Engineering, London South Bank University, London, SE1*

† Corresponding author: Shahriar Sajjadi

Email: *shahriar.sajjadi-emami@kcl.ac.uk*

Keywords: Microfluidics; Alginate microfibers; Encapsulation

Abstract

A unified microfluidic approach is presented for flexible fabrication of oil-encapsulated calcium alginate microfibers. The oil encapsulate phase was directly injected into the gelling alginate fiber, thus allowing the adjustable tuning of the encapsulate geometry ranging from spherical to prolate ellipsoid, plug-like and tubular shapes. Phase maps were developed that show the conditions required to achieve desired fiber morphologies with intended encapsulate phase ratio. We also show for very first time how oil encapsulates can be selectively grouped across the microfibers. A force-balance model, validated against a non-gelling system, was introduced to predict the size of spherical encapsulates.

1. Introduction

Sodium alginate is a naturally-occurring and biocompatible water-soluble material which forms hydrogel when cross-linked with calcium ions. Calcium alginates are widely used for various biomedical and pharmaceutical applications. In particular, calcium alginate in the form of microfibers has found

increasing biomedical applications such as in wound healing [1-3], cell encapsulation [4] and tissue engineering [5]. These fibers are usually produced via wet spinning technique [6], in which an aqueous sodium alginate solution is injected into an aqueous calcium chloride solution, where the jet of alginate solution is gelled by the Ca^{2+} ions from the aqueous solution to form a fibrous structure.

The properties of alginate microfibers can be further enhanced by introducing compositional [7] and geometrical [8] heterogeneity, or embedding different inorganic additives in the hydrogel matrix of the fiber, such as silver compounds [9-11], or coating the fibers with active materials [12]. Alternatively, different aqueous as well as non-aqueous solutions can be encapsulated within the fiber to increase its functionalities. For example, an aqueous medium containing proteins and cells can be loaded within alginate fibers in a tubular fashion, and used in tissue engineering applications for mimicking and reconstruction of fibre-shaped functional tissues [13]. On the other hand, alginate fibers containing non-aqueous phases [14-18] have also shown a number of features, such as improved water collection ability [19], which has been attributed to multiple factors including the increase in Laplace force due to curvature gradient around the encapsulated-oil nodes. In general, both encapsulation geometries, tubular and segmented, have unique advantages and applications. However, the encapsulation geometry produced by current encapsulation techniques is severely limited by the nature of the dispersed phase used. Namely, a non-aqueous dispersed phase can only be loaded in discrete segments, while an aqueous dispersed phase is restricted to a tubular encapsulation.

In this report, we introduce a unified and flexible microfluidic technique for oil encapsulation within alginate fibers, by which the encapsulation geometry can be precisely tuned from continuous tubular to equally spaced segments including plugs, ellipsoids and spheres across the microfibers. This is also the first report in the literature on the fabrication of microfibers with controlled grouped oil encapsulates. We show how encapsulation volume may be compromised

for achieving a desired morphology. Lastly, we introduce a physical force-balance model, validated against gelling and non-gelling systems, which can predict the size of oil encapsulates.

2. Experimental Section

2.1 Materials

Sodium alginate and calcium chloride (Sigma Aldrich) were used as received. Distilled water was used as the middle and external phase. Octane (99%, Sigma Aldrich) was used as received as the model inner-oil encapsulated phase. A water-soluble dye (trypan blue) was used in the alginate phase for mapping.

2.2 Device and Procedure

Figure 1a shows a schematic of the microfluidic device used to encapsulate oil phase within the alginate fiber. Two glass capillaries (CM Scientific, UK), circular (ID: 0.56 mm, OD: 1 mm) and square (IL: 1 mm, OL: 1.5 mm), were pulled using a pipette puller (P-1000, Sutter Instrument, Novato, USA).The tapered tips were cut to the desired sizes, with the inner tip (ID: 40 µm, OD: 60 µm) aligned symmetrically with the outer tip (ID: 150 µm, OD: 175 µm). Both capillaries were plasma treated (Femto Plasma Cleaner, Diener) to be hydrophilic. To make the inner capillary hydrophobic, its glass surface was exposed to the vapors of n-Octadecyltrimethoxysilane inside an oven at 130˚C for 15 minutes, followed by its cooling down at room temperature for one hour. The oil phase was pumped (Harvard Apparatus) through the inner capillary, while the alginate phase was introduced through the interstitial spaces between the two capillaries. The outer aqueous phase containing calcium chloride was kept quiescent, in which the coaxially aligned capillary setup (Figure 1b) was introduced vertically as shown in Figure 1a. The formed fibers were collected at the top of the cuvette, facilitated by the buoyancy force exerted by the encapsulated oil. This buoyancy-assisted microfluidic setup has previously been used to produce

dehydration-responsive oil-loaded alginate microfibers [20], and to generate millimetric core-shell drops with tunable shell thickness [21,22]. A high-speed video recording camera (Photron FastCam SA-5 monochrome) was used to record fiber formation. The middle water phase containing sodium alginate (1.0 and 4.0 wt. %), was introduced into an outer aqueous solution containing 4.0 wt% calcium chloride at different flow rates to form fibers.

The interfacial tension between 1wt% aqueous solution of alginate and the octane oil phase, measured using DCA-100 (First Ten Angstrom) device via Du Nouy ring technique, was found to be 20.1 mN/m. The viscosity of the aqueous 1 wt% alginate solution, measured using ARES Rheometer via the double-couette flow technique, was found to be 14.33 mPas.

3. Results and Discussion

3.1 From Segmented to Tubular Oil Encapsulation

Both aqueous and non-aqueous fluids can be encapsulated in calcium alginate microfibers. An aqueous inner phase is usually encapsulated in a tubular configuration due to extremely low interfacial tension [15]. However, a hydrophobic inner phase is usually encapsulated in discrete segments [14,15] due to the high interfacial tension at oil-water interface acting to rupture the inner phase. We present a one-step microfluidic approach that allows to achieve both segmented and tubular oil encapsulations by using a single device in which the tip of capillary carrying the oil phase is kept at the same level as that of the outer capillary. This is different from the conventional approach where the inner tip is placed upstream [14,15].

Figure 1c shows the evolution of fiber morphology from fibers encapsulating discrete oil segments as spheres, prolate ellipsoids (referred to as *ellipsoid* for simplicity) and plug-like to eventually a single straight tube filled up with oil, all obtained via increasing the inner oil phase volumetric flow rate (Q_{oil}) at a constant middle alginate phase flow rate (Q_{alg}). It is evident that the volume of dispersed oil phase increases with Q_{oil} [23-25]. However, the increase in the oil

segment volume may alter its shape because of geometrical constraints imposed by the gelling shell, as seen in Figure 1c. At high Q_{oil}, the oil encapsulate cannot be accommodated within the fiber as a spherical droplet because of the restrictions imposed by the gelling alginate phase, as a result it expands axially within the fiber (in the direction of fiber length) to form an ellipsoidal entity. Further increase in Q_{oil} only elongates the ellipsoidal segments axially within the fiber, thus leading to the formation of plug-like oil segments. When Q_{oil} is significantly increased, the inner oil phase ceases to rupture into discrete entities, thereby forming a continuous tubular jet inside the fiber.

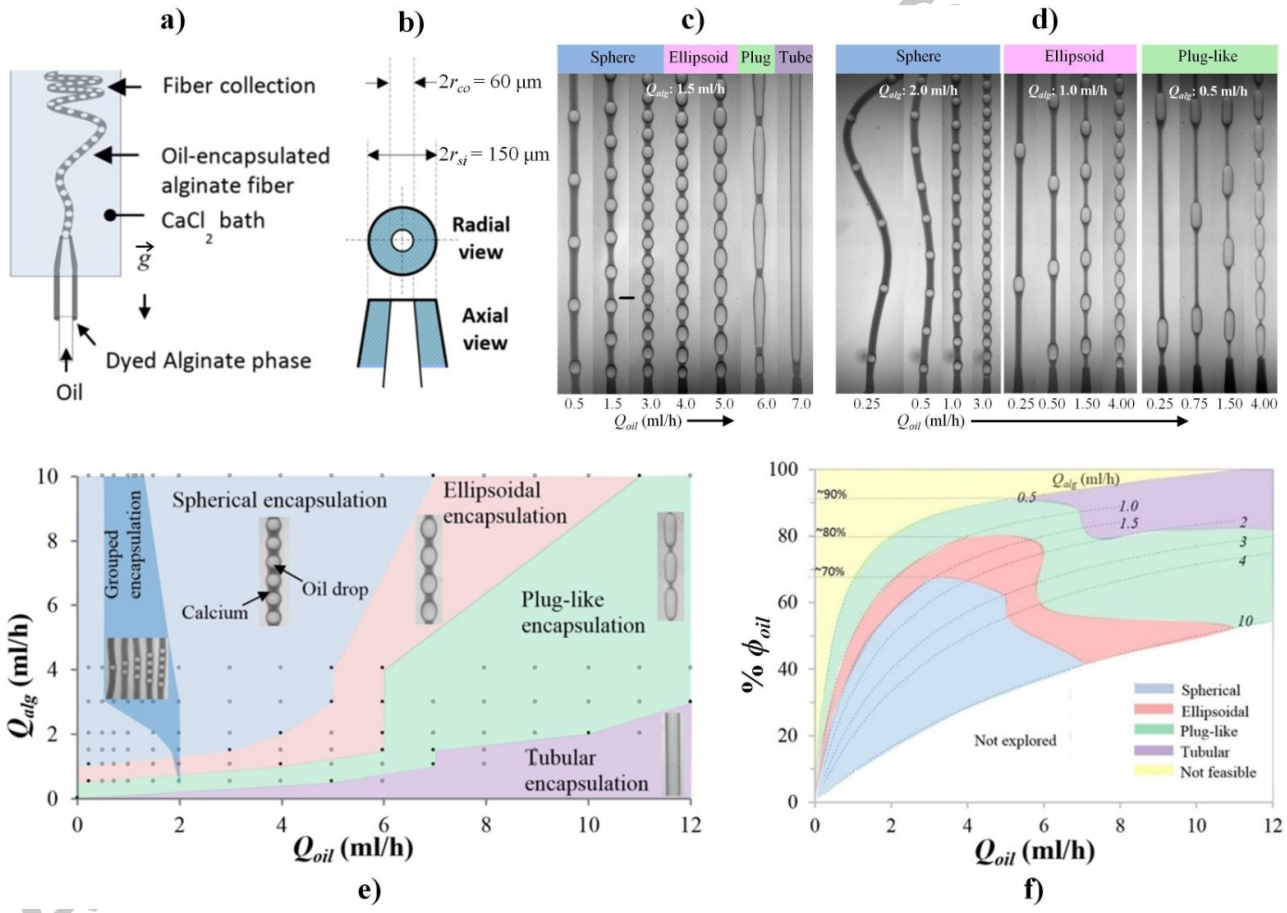

Figure 1 a) A schematic of the microfluidic device used for producing oil-encapsulated alginate fiber (a1). **b)** The symmetrically aligned coaxial capillary setup used. r_{co}: outer radius of inner capillary, r_{si}: inner radius of outer capillary. **c)** Variations in the shape of oil segments encapsulated within the alginate fibers with increasing the inner-oil phase flow rate (Q_{oil}). The figure shows that the nature of encapsulation can be switched between a segmented encapsulation

(having spherical, ellipsoidal or plug-like shapes) and a continuous (tubular) encapsulation. Scale bars: 200 µm. **d)** Variation in the inter-droplet distance with Q_{oil} while the size and shape of encapsulated droplets were maintained. The inter-droplet distance decreases by increasing Q_{oil} for all the drop shapes. **e)** A phase map showing diverse shapes of the encapsulated oil phase within the alginate fibers obtained for different middle-alginate phase flow rate (Q_{alg}) and Q_{oil}. The circular symbols indicate the experimental data points explored, while the filled symbols indicate the data points lying at the transition boundaries between the different shapes. The boundaries between Q_{alg} = 4 and 10 ml/h are approximated. **f)** Oil-volume encapsulation percentage achieved for different encapsulate shapes versus Q_{oil}. Solid lines indicate the fixed Q_{alg} conditions. All data obtained for 1 wt% alginate and 4 wt% $CaCl_2$ concentrations.

Figure 1d also shows some conditions under which morphology changes did not occur and all morphologies, from sphere to ellipsoid and plug-like encapsulates, could simply be maintained while altering Q_{oil} and Q_{alg}. This dilemma is resolved by Figure 1e, which shows the phase map for different shapes of oil encapsulates obtained by a two-dimensional Q_{alg} versus Q_{oil} scan. The sequence of morphological evolution with Q_{oil}, whose path is from sphere, ellipsoid, plug-like to tubular, remained the same for all flow conditions studied. The only exception was at low Q_{alg} where it was possible to bypass the spherical and elliptical morphologies and move directly to plug-like and tubular due to low drag. Note that the tubular structures can be achieved for Q_{alg} > 4.0 ml/h too, but at a much higher Q_{oil} than that explored in the map. At rather low Q_{oil} and high Q_{alg}, indicated by the light blue zone in the phase map, the encapsulated oil takes spherical shape because the droplet size remains small relative to the fiber thickness. Within this region, the droplets reduce in size with increasing Q_{oil}, but at a fixed Q_{alg}, while maintain their spherical shape. The dark blue region on the map, which relates to grouped oil encapsulation, is discussed later.

As the change in oil volume is often associated with a change in segment morphology, a trade-off exists between preserving the desired oil entity's shape and maximising the encapsulation volume. Figure 1f shows a plot between the % oil volume encapsulated in a fiber, $\phi_{oil} =$

$\left(\frac{Q_{oil}}{Q_{oil}+Q_{alg}} \times 100\right)$, and Q_{oil} for different alginate phase flow rates. We noted that there are narrow ranges of flow conditions within which the desired segment morphologies can be preserved. Within these specified regions, the encapsulation volume can be fine-tuned by altering Q_{oil} without affecting the fiber shape (Figure 1d). Figure 1f also shows that for a fiber with given encapsulation ratio, there exists a number of possible morphologies. However, the optimum morphologies should be chosen based on the intended use of the fibers and specific properties sought. Figure 1f reveals that the maximum ϕ_{oil} achievable for different fiber morphologies are in the ascending order of ~70% for spherical, ~80% for ellipsoidal, ~90% for plug-like, and >90% for tubular. The yellow region was found to be non-feasible because the alginate phase gelled and blocked the capillary tip at low flow rates.

3.2 Grouping of Encapsulated Droplets

We discovered that the affinity of the inner glass capillary, which carries the oil phase, can affect the regular formation of oil droplets within the fiber. This observation was exploited to activate the grouping of oil encapsulates within the fiber in a controllable manner. A hydrophilic inner capillary can facilitate the grouping of oil encapsulates within a certain range of flow conditions, shown as a dark blue region in Figure 1e. The number of entities in a group can be precisely controlled via fine tuning the flow conditions, as shown in Figure 2a, for different encapsulate morphologies (Figure 2b). Such controlled grouping of encapsulated oil entities could be useful for local tuning of the fiber structure. It also provides defect-free bending points along the fiber, which could minimize the risk of accidental shell rupture and the associated oil release.

The mechanism of grouping behavior was found to be a result of the temporary blockage of hydrophilic inner capillary tip with the alginate phase, which only occurred at low oil phase flow rates. Once an oil droplet is formed, the capillary pressure at the tip reduces to a minimum value. At this reduced pressure, the aqueous alginate phase is able to enter and wet the inner hydrophilic

surface by forcing the oil phase to temporarily recede inside the capillary, as can be observed in dye-free fibers (Figure 2c2).

The pressure build-up with time inside the capillary would eventually push the intruded alginate phase out of the inner capillary along with the oil phase. This results in a rapid outpour of a large volume of the oil phase, which ruptures into uniform multiple oil encapsulates under the influence of the drag force exerted by the middle phase. The upper limit of the built-up pressure increases with Q_{oil}, which increases the volume of oil being pumped out at the instance of pressure release. This increases the number of oil entities in a group with Q_{oil}, as shown in Figure 2a. This cycle of the pressure build-up and release at the tip of a hydrophilic inner capillary leads to the grouped formation of the oil encapsulates. At a high Q_{oil}, the alginate phase fails to push the oil in and, as a result, regular oil encapsulates are formed.

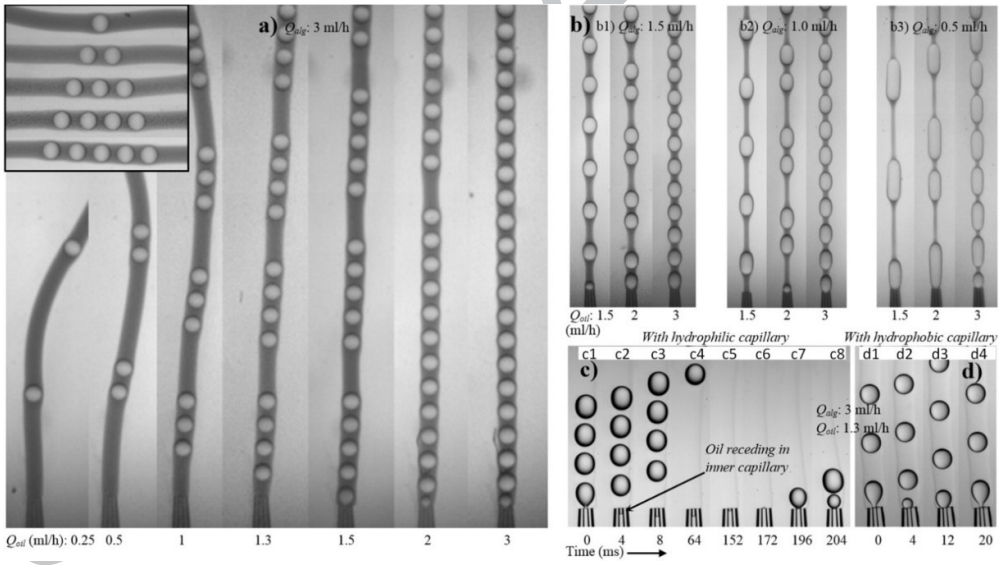

Figure 2 a) Precise grouping of the spherical oil droplets in the microfibers with varying Q_{oil} by employing a hydrophilic inner capillary. This grouping phenomenon can also be achieved for plug-like and ellipsoids, as shown in **(b)**. The mechanism of grouping behavior is analyzed with time-evolution images of dye-free fibers shown in **c)**, while the grouping behavior can be muted by using a hydrophobic inner capillary (**d)**.

In order to demonstrate that this grouping phenomenon can be deactivated on demand, a similar device with a hydrophobic inner capillary (having identical dimensions) was fabricated and used to produce fibers under identical conditions. The grouping phenomena ceased to exist for this device, as the alginate phase did not tend to wet the inner capillary. This prevented the receding of oil phase inside capillary, and hence eliminated the grouped formation of the oil entities. Figure 2d shows that the microfibers obtained under identical flow conditions from the device having a hydrophobic inner capillary display no grouping behavior. The oil entities for both grouped and ungrouped fibers were stable and remained inside the fibers in the hydrated state and after dehydration for several months, if the fibers were highly crosslinked.

3.3 Fiber morphologies and dimensions

The nomenclatures for a compound fiber are shown in Figure 3a. Figures 3b-3d show the size data for the minimum fiber thickness (t), the minor axis of oil segments d (referred to as *radial diameter*) and the fiber length between consecutive segments (z). Figure 3e reveals the fibers roughness (t/T), where T is the maximum fiber thickness around the oil segment. A $t/T = 1.0$ signifies flat fibers. Similarly, the geometry of encapsulated oil segments can be represented by the dimensionless term d/D as shown in Figure 3f. A $d/D = 1.0$ indicates spherical geometry for encapsulates. All data points in Figure 3b-3f are shown in terms of Q_{oil}.

The minimum diameter of fibers t varied only slightly with Q_{oil}, but increased considerably with Q_{alg} (Figure 3b), which is consistent with previous observations [15]. The segment's radial (d) and axial (D) diameters, which determine the volume of oil entities, remained constant at low Q_{oil} (Figure 3c and 3f) where the segments were separated by long alginate threads (z) in between (Figure 3d). At low Q_{oil}, a high Q_{alg} kept the entity small and therefore spherical (Figure 3f, $d/D \approx 1$) due to high drag exerted by the middle phase. The size of these spherical oil segments can be predicted by a simple force-balance model, which is explained later. A small increase in Q_{oil} in

such conditions did not increase the segment volume, but increased its frequency, thereby reducing the alginate thread length z.

However, the volume of encapsulated entity increased with further increase in Q_{oil}. This is because an increase in Q_{oil} directly increases the drop expansion velocity (v_d) and thus reduces the disruptive drag force, which is proportional to (v_d -v_m), where v_m is the middle phase velocity. As the cross-sectional area for the inner oil phase was significantly smaller than that for the middle phase, a small increase in Q_{oil} was always translated into a larger reduction in the disruptive drag force.

The large oil segments could not significantly bulge the gelled interface radially, as indicated by the nearly flat t/T curves for a fixed Q_{alg} (Figure 3e), therefore expanded themselves in axial direction considerably, leading to an increase in D (Figure 3f).

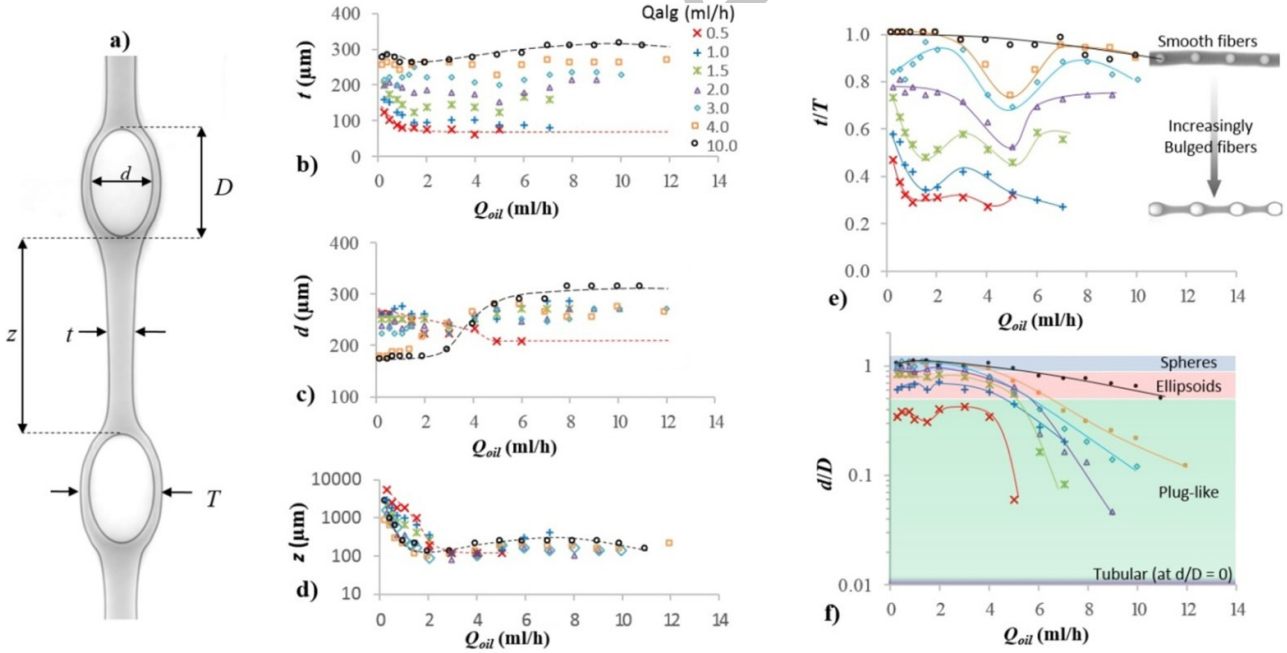

Figure 3 The assigned nomenclatures to various dimensions of an oil-encapsulated fiber are shown in **(a)**. Variations in the minimum fiber thickness (t), the radial diameter of oil segments (d) and the axial length of fiber segment (z) versus Q_{oil} are shown in **(b)**, **(c)** and **(d)**, respectively. The variations in dimensionless parameters t/T and d/D are presented in **(e)** and **(f),** respectively, against Q_{oil} at different Q_{alg}. The red and black dashed trend lines in (b), (c) and (d) indicate the

minimum and the maximum Q_{alg} used, respectively. The common legends for figures (b-f) are shown in (b).

The increase in D reduced z to a minimum as the oil segments were tightly packed against each other (Figure 3d). This increase in D also shaped the segments from spherical to ellipsoids and plug-like, until a tubular oil entity was eventually reached at high Q_{oil} (Figure 1c and Figure 3f). As the shape of oil segments evolved with Q_{oil}, the fiber surface morphology changed correspondingly. Smooth fibers were obtained at high Q_{alg} due to large t (Figure 3e, $t/T \approx 1$), irrespective of the encapsulated segment shape. The local minima in the curves correspond to conditions where shape transition of the oil segments occurred.

3.4 Size estimation and analysis

A theoretical force-balance model is presented for predicting the volume of oil segments encapsulated in the alginate fiber. While the model can theoretically be extended to all types of segments, we limit our discussion to spherical oil segments (Figure 4a) due to the simplicity involved in drag force estimation. Four different forces act on an oil droplet during its formation: kinetic force (F_k), drag force (F_d), buoyancy force (F_b) and interfacial force (F_σ).

Of these forces, only the interfacial force acts cohesively, which tends to keep the drop attached to the capillary tip. The expressions for these forces are presented below.

$$F_k = \rho_{oil}\, Q_{oil}\, u_{oil} \tag{1}$$

$$F_\sigma = 2\pi\, r_w\, \sigma \tag{2}$$

$$F_b = \Delta\rho\, g\, \pi\, (d_{oil})^3/6 \tag{3}$$

$$F_d = 6\pi\, \eta_{alg} \Delta v\, d_{oil}/2 \tag{4}$$

where ρ_{oil} and u_{oil} represent the density, and velocity of the inner oil phase, respectively. The r_w and d_{oil} are the wetting radius of the oil droplet at the inner capillary tip, and the oil droplet diameter, respectively.

The σ represents the interfacial tension, while the η_{alg} stands for the alginate phase viscosity. The term $\Delta v = v_m - v_d$, with v_m being the average middle alginate phase velocity at the tip cross section (outer tip- inner tip cross section), and v_d, the velocity of the expanding drop, also defined as the instantaneous droplet velocity, which was calculated as $\Delta(d_{oil})/\Delta t$ with $\Delta t \rightarrow 0$. The droplet velocity v_d increases with the inner phase velocity which is equal to $Q_{oil}/\pi r_{ci}^2$, while the middle phase velocity is calculated as $Q_{alg}/\pi(r_{ci}^2 - r_{co}^2)$, where r_{ci} and r_{co} are the inner and outer radius of the core capillary, and r_{si} is the inner radius of the shell capillary at the tip level, as defined in Figure 1b.

The resulting force balance equation can be expressed as,

$$F_\sigma = F_k + F_b + F_d \quad (5)$$

Equations 1-5 were solved iteratively for d_{oil} by incrementally increasing d_{oil} from zero with a step resolution of 0.01 µm until a value satisfying Equation 5 was found. We have previously used a similar model to predict the droplet size in a buoyancy assisted co-flow systems [21,22]. However, the significance of the current system is that the viscosity of alginate phase varies with time, which is hard to predict.

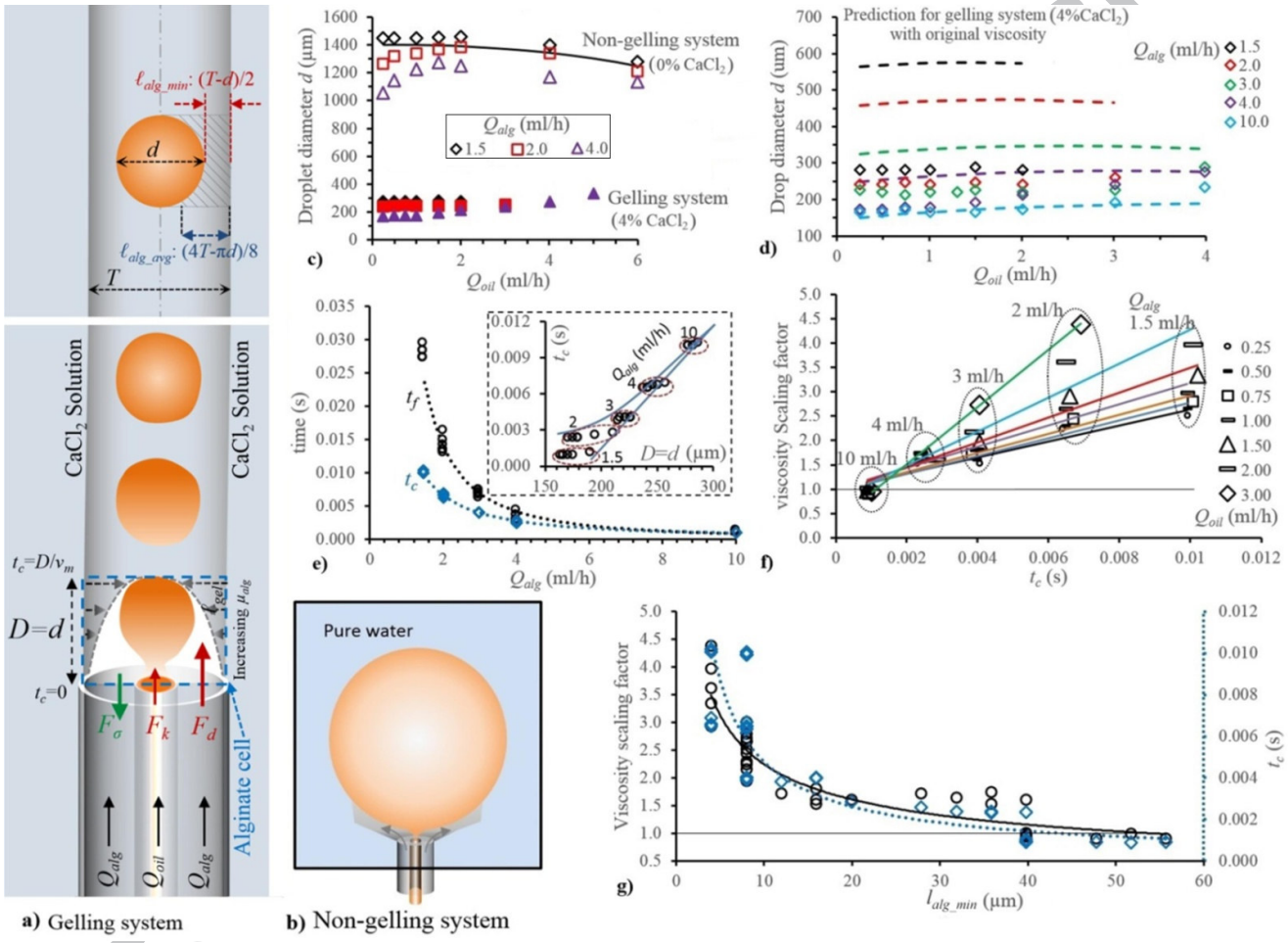

Figure 4 a) A schematic showing the forces applied to an emerging oil drop inside a gelling alginate fiber, and the minimum $\left(\ell_{alg\_min} = \frac{T-d}{2}\right)$ and the average $\left(\ell_{alg\_avg} = \frac{4T-\pi d}{8}\right)$ alginate shell thickness. **b)** A schematic showing the formation of large oil drops in the absence of $CaCl_2$ (non-gelling system) in the outer aqueous phase. **c)** The graph shows the effect of gelation of alginate phase on the oil drop size, where the droplets formed at 0% $CaCl_2$ (non-gelling system) and 4.0 % $CaCl_2$ (gelling system) are compared. The solid black line shows the drop size predictions for a non-gelling system when the drag exerted by the middle phase flow was completely neglected. **d)** Drop size predictions for a gelling system using the original viscosity value of the alginate phase. **e)** The

comparison of the characteristic cell-contact time (t_c) and the drop formation time (t_f) plotted against Q_{alg}. **e)** The reverse-calculated viscosity scaling factors (S_η) using the model illustrated in (a) are plotted against t_c for different Q_{oil} and Q_{alg}. **g)** The S_η (primary axis) and t_c (secondary axis) show a similar correlation against ℓ_{alg_min}.

In order to validate the model, we conducted a number of runs in the absence of $CaCl_2$ in the outer phase (i.e., non-gelling system). Figures 4a-4b show the schematics for drop formation in gelling and non-gelling systems.

The impact of gelation on the size of oil segments is illustrated in Figure 4c, which compares the droplet sizes obtained for the gelling system (with 4.0 wt% $CaCl_2$) with those for the non-gelling system (with 0 wt% $CaCl_2$). There is a significant difference between the scales of drag forces acting on drops in these two cases. In the absence of gelation, the middle alginate phase expanded around the forming oil droplet and into the outer aqueous phase, thereby minimizing the drag exerted on the droplet and thus allowing it to grow in size before rupture. Not only the droplet size in the non-gelling case was much larger than that in the gelling case, but was even larger than the size of the outer tip, which sets the size of the jet. However, in the case of reacting gels, the gelling interface provided a confinement, which acted as a virtual extension of the outer capillary for the growing oil droplet. This allowed the middle alginate phase to flow through the virtual pipe and exert roughly the same magnitude of drag on the oil droplet as it would do if the inner tip was placed upstream.

We first applied the model to the non-gelling system at a low alginate phase flow rate (Q_{alg} = 1.5 ml/h). By using the non-gelling system, we ensured that viscosity of the alginate phase remained constant (14.33mPas), avoiding the complexity associated with variations in the alginate viscosity with time during gelation. A low Q_{alg}, 1.5 ml/h, was initially selected to nullify the shear stress (drag) acting on the oil phase, allowing us to neglect the drag term from Equation 5. This further simplified the model by avoiding the inaccuracy involved in the estimation of the drag at the tip level due to the escaping middle phase. The simplified model was still able to accurately predict the drop sizes (black line), as shown in Figure 4c.

For higher Q_{alg} values of 2 and 4 ml/h, however, the effect of the drag manifested itself as a maximum in droplet size data. Prior to the maximum, the droplet size increased with increasing Q_{oil} due to decreasing drag; $\eta_{alg} = (v_m - v_d)$. At the maximum, the decrease in disruptive drag force with increasing Q_{oil} was balanced by an equal increase in disruptive kinetic force (Eq.1). After the maximum, the kinetic force became dominant, giving a similar droplet trajectory predicted by the model for Q_{oil} = 1.5 ml/h. Note that the model was not applied to high Q_{alg} values under non-gelling condition, for the reasons discussed earlier.

The physical model was then applied to the gelling system where the viscosity experienced by oil drops is a function of diffusion rate of calcium ions into the alginate phase, flow rates and the concentration of two reactants. One can expect that for very high alginate phase flow rate, where the convective rate of transport of alginate phase is much greater than the diffusion rate of calcium ions, there will be little change in the viscosity of alginate phase at the tip where drops form. Figure 4d compares the calculated results (dashed lines) using the original viscosity of the alginate phase (14.33mPas) versus experimental data (data points). It can be seen that the predictions fit very well with the experimental data at high Q_{alg} (10 ml/h), but significantly over-estimated the drop size at low Q_{alg} values. This indicates that the proposed model can directly be used to predict the size at high Q_{alg} ($\geq$ 10 ml/h) where the change in viscosity, due to gelation at the tip during oil-drop formation, is negligible.

The importance of dynamic viscosity for Q_{alg} < 10 ml/h cannot be further overemphasized than by the difference between the predicted results, using the original viscosity of the alginate phase (14.33mPas), and the experimental data, as shown in Figure 4d. While the model was still able to predict the trend with Q_{oil} and Q_{alg}, it failed to predict the drop size by a great margin.

Before oil droplets start to experience the change in the viscosity of the media they are dispersed in, calcium ions have to diffuse from the outer calcium chloride solution to the droplets. The diffusion of calcium ions into the moving alginate phase, which is also associated with concomitant gelation, causes a progressing gel front to form, which changes the viscosity of the alginate phase.

We define a characteristic time for the progression of the gel front during drop formation. At the instance of drop detachment, when the force balance defined by Eqs. 1-5 is valid, the alginate phase has travelled a characteristic distance of D=d (for spherical droplet) at the velocity of v_m, as shown in Figure 4a. This means that the alginate cell, engulfing a detaching droplet, can be defined by a characteristic "cell contact time" of $t_c = D/v_m$ at the leading surface, and $t_c = 0$ at the lagging surface at the capillary tip level. The contact time indicates the effective time during which the alginate phase cell has been exposed to calcium ions from the external water phase, and as a result the gel front has progressed from the calcium chloride-sodium alginate boundary towards the centre of alginate fibers in the cell.

The relationship between D and t_c, as shown in Figure 4e inset, becomes linear at high Q_{alg}. It follows that the gel front, whose length defined by ℓ_{gel}, is maximum at the top surface and minimum at the bottom surface of the cell, with a decreasing trajectory in between depending on the kinetics of gelation. We now define ℓ_{alg} as the thickness of the alginate phase (including both sol and gel) around an encapsulate so that $(T-d)/2 < \ell_{alg} < T/2$. For a spherical droplet, the alginate thickness is minimum at the centreline of the droplet (ℓ_{alg_min}), but is maximum at the top and bottom of the cell enclosing the droplet (Figure 4a). The average value of ℓ_{alg} across the length of an emerging drop with diameter d can be calculated as $(4T-\pi d)/8$. However, we assume ℓ_{alg} can be represented by ℓ_{alg_min} because it has the biggest impact on the droplet formation.

There is also a characteristic time for droplets to form; droplet formation time t_f which is defined by v_{oil}/Q_{oil}. This is the time during which an oil droplet is attached to the micro capillary tip and exposed to the passing alginate stream. Larger oil droplets obtained at low Q_{alg} have longer formation and cell contact times, and are more likely to be affected by the progressing gel front.

In contrast, for small droplets obtained at high Q_{alg}, the cell-contact time t_c becomes equal to the drop formation time t_f. Figure 4e clearly shows that at low Q_{alg}, the actual contact time of an emerging droplet with its cell, before its detachment, is much shorter than its formation time. Therefore, the properties of the media cell engulfing the drop at the onset of detachment is only set

at a fraction of t_f. However, the difference decreased exponentially with increasing Q_{alg} (Figure 4e), due to a decrease in drop size, until both characteristic times converged, indicating that the drag is so dominant at high Q_{alg} that the droplet and its cell moved uniformly and simultaneously.

Having already ensured the validity of the model for cases with no significant change in the viscosity of the alginate phase, we reverse-calculated the required effective viscosity of the alginate phase to reproduce the size data. Figure 4f shows the variations in the viscosity scaling factor (S_η), normalized effective viscosity relative to the viscosity of the alginate phase, with the cell contact time for different Q_{alg} and Q_{oil}. A scaling factor of up to 4.5 was found to be sufficient to address the viscosity increase of the alginate phase during gelation. The viscosity scaling factor scaled linearly with the characteristic cell contact time, with the slope depending on the oil phase flow rate (Figure 4a). Furthermore, Figure 4f shows that a low Q_{alg} is associated with a high effective viscosity. This is because with an increase in the drop size, and as a result in the cell contact time, the sol alginate shell reduced in thickness as the gel front progressed further. This implies a shorter distance between the droplet surface and the gel front, $\ell_{alg} - \ell_{gel}$, and a higher effective viscosity. By relating ℓ_{alg} with droplet size, one can conclude that the effective viscosity of the alginate increased with increasing Q_{oil} while decreased with increasing Q_{alg}.

Figure 4g shows variations in S_η and t_c with ℓ_{alg}. It is interesting to note that ℓ_{alg} correlates with t_c as $\ell_{gel} \propto t_c^{1/2}$, in a similar way that the gel front ℓ_{gel} has been reported to correlate with time at $CaCl_2$ concentrations similar to the one used in this work; $\ell_{gel} \propto t_c^{1/2}$ [26]. This may suggest that $\ell_{alg} \approx \ell_{gel}$; the gel front reaches the surface of evolving drops at low Q_{alg}. It is not easy to calculate the effective viscosity of a heterogeneous media (with an overall length ℓ_{alg}) composed of a gel front with length ℓ_{gel} and an aqueous solution of alginate phase with length $\ell_{alg} - \ell_{gel}$ in order to predict droplet sizes. However, we were able to show that the effective viscosity scales with ℓ_{alg}, which can be expressed as $S_\eta \propto (\ell_{alg})^{-1/2}$ (Figure 4g).

4. Conclusion

A facile microfluidic approach was introduced for flexible oil encapsulation in alginate microfibers, which was based on the simultaneous formation and encapsulation of the oil phase. Using this method, one is able to tune the encapsulate shape across a wide spectrum of geometries (spherical, ellipsoidal, plug-like and tubular). The encapsulated oil entities were also selectively grouped by varying the surface affinity of the oil-injecting capillary. A hydrophilic inner capillary activated the grouping mechanism, while the number of droplets per group could be adjusted by the oil phase flow rate (Q_{oil}). The grouping phenomenon could also be switched off by treating the inner capillary to be hydrophobic.

A fundamental physical force-balance model was also introduced to predict the size of spherical encapsulates. The proposed model accurately predicted the size of droplets formed in a non-gelling system, which ensured the validity of the model, as this system avoided the complexity associated with variations in the alginate viscosity during gelation. In case of a gelling system, the model correctly predicted the size of droplets formed at high alginate phase flow rates (Q_{alg}), where the viscosity of the alginate cell engulfing emerging oil drops did not change appreciably due to the high velocity of alginate phase (i.e., short drop formation time). The significance of dynamic viscosity at low Q_{alg} was studied by comparing the droplet formation time (t_f) against the cell contact time (t_c), during which the alginate gel front progressed towards the droplet inside the fiber. At low Q_{alg} large spherical droplets with maximum t_c and minimum alginate thickness (ℓ_{alg}) were formed. This resulted in an approximately five-fold increase in the alginate phase viscosity at the capillary tip during drop formation, compared to its original viscosity.

5. Acknowledgements

We acknowledge the use made of Photron FastCam SA-5 (monochrome) high-speed video recording system, which was borrowed from the EPSRC (Engineering and Physical Sciences and Research Council) Engineering Instrument Pool.

References

[1] R. Mahsood, M. Miraftab, Novel materials for moist wound management: Alginate-psyllium hybrid fibres, *J. Wound Care* 23 (2014) 3 153-159.

[2] J. Sun, H. Tan, Alginate-based biomaterials for regenerative medicine applications, *Materials* 6 (2013) 4 1285-1309.

[3] S.Y. Ahn, C.H. Mun, S.H. Lee, Microfluidic spinning of fibrous alginate carrier having highly enhanced drug loading capability and delayed release profile, *RSC Adv.* 5 (2015) 20 15172-15181.

[4] H. Onoe, S. Takeuchi, Cell-laden microfibers for bottom-up tissue engineering, *Drug Discov. Today* 20 (2015) 2 236-246.

[5] M.A. Daniele, D.A. Boyd, A.A. Adams, F.S. Ligler, Microfluidic strategies for design and assembly of microfibers and nanofibers with issue engineering and regenerative medicine applications, *Adv. Healthcare Mater.* 4 (2015) 1.

[6] J. Su, Y. Zheng, H. Wu, Generation of alginate microfibers with a roller-assisted microfluidic system, *Lab Chip* 9 (2009) 7 996-1001.

[7] Y. Cheng, Y. Yu, F. Fu, J. Wang, L. Shang, Z. Gu, Y. Zhao, Controlled Fabrication of Bioactive Microfibers for Creating Tissue Constructs Using Microfluidic Techniques, *ACS Appl. Mater. Interfaces* 8 (2016) 2 1080-1086.

[8] Y. Zhang, Y. Tian, L.L. Xu, C.F. Wang, S. Chen, Facile fabrication of structure-tunable bead-shaped hybrid microfibers using a Rayleigh instability guiding strategy, *Chem. Comm.* 51 (2015) 17525-17528.

[9] Y. Qin, Silver-containing alginate fibres and dressings, *Int. Wound J.* 2 (2005) 2 172-6.

[10] C. Trial, H. Darbas, J. Lavigne, A. Sotto, G. Simoneau, Y. Tillet, L. Teot, Assessment of the antimicrobial effectiveness of a new silver alginate wound dressing: a RCT, *J. Wound Care* 19 (2010) 1 20-26.

[11] K. Neibert, V. Gopishetty, A. Grigoryev, I. Tokarev, N. Al-Hajaj, J. Vorstenbosch, A. Philip, S. Minko, D. Maysinger, Wound-healing with mechanically robust and biodegradable hydrogel fibers loaded with silver nanoparticles, *Adv. Healthcare Mater.* 1 (2012) 5 621-630.

[12] L. Shang, F. Fu, Y. Cheng, Y. Yu, J. Wang, Z. Gu, Y. Zhao, Bioinspired Multifunctional Spindle-Knotted Microfibers from Microfluidics, *Small* (2016) DOI:10.1002/smll.201600286.

[13] H. Onoe, T. Okitsu, A. Itou, M. Kato-Negishi, R. Gojo, D. Kiriya, K. Sato, S. Miura, S. Iwanaga, K. Kuribayashi-Shigetomi, Y.T. Matsunaga, Y. Shimoyama, S. Takeuchi, Metre-long cell-laden microfibres exhibit tissue morphologies and functions, *Nat. Mater.* 12 (2013) 6 584-590.

[14] Y. Yu, H. Wen, J. Ma, S. Lykkemark, H. Xu, J. Qin, Flexible fabrication of fiomimetic bamboo-like hybrid microfibers, *Adv. Mater.* 26 (2014) 16 2494-2499.

[15] X. He, W. Wang, K. Deng, R. Xie, X. Ju, Z. Liu, L. Chu, Microfluidic fabrication of chitosan microfibers with controllable internals from tubular to peapod-like structures, *RSC Adv.* 5 (2015) 2 928-936.

[16] E. Um, J.K. Nunes, T. Pico, H.A. Stone, Multicompartment microfibers: fabrication and selective dissolution of composite droplet-in-fiber structures, *J. Mater. Chem. B* 2 (2014) 45 7866-7871.

[17] T. Sun, C. Hu, M. Nakajima, M. Takeuchi, M. Seki, T. Yue, Q. Shi, T. Fukuda, Q. Huang, On-chip fabrication and magnetic force estimation of peapod-like hybrid microfibers using a microfluidic device, *Microfluid. Nanofluid.* 18 (2015) 5-6 1177-1187.

[18] X. Ji, S. Guo, C. Zeng, C. Wang, L. Zhang, Continuous generation of alginate microfibers with spindle-knots by using a simple microfluidic device, *RSC Adv.* 5 (2015) 2517-2522.

[19] X. He, W. Wang, Y. Liu, M. Jiang, F. Wu, K. Deng, Z. Liu, X. Ju, R. Xie, L. Chu, Microfluidic fabrication of bio-Inspired microfibers with controllable magnetic spindle-Knots for 3D assembly and water collection, *ACS Appl. Mater. Interfaces* 7 (2015) 31 17471-17481.

[20] A.S. Chaurasia, S. Sajjadi, Flexible asymmetric encapsulation for dehydration-responsive hybrid microfibers, *Small* 12 (2016) 30, 4146-4155.

[21] A.S. Chaurasia, S. Sajjadi, Millimetric core-shell drops via buoyancy assisted non-confined microfluidics, *Chem. Eng. Sci.* 129 (2015) 260-270.

[22] A.S. Chaurasia, D.N. Josephides, S. Sajjadi, Large Ultrathin Shelled Drops Produced via Non-Confined Microfluidics, *Chemphyschem* 16 (2015) 2, 403-411.

[23] C. Cramer, P. Fischer, E.J. Windhab, Drop formation in a co-flowing ambient fluid, *Chem. Eng. Sci.* 59 (2004) 15 3045-3058.

[24] S.A. Nabavi, G.T. Vladisavljevic, S. Gu, E.E. Ekanem, Double emulsion production in glass capillary microfluidic device: Parametric investigation of droplet generation behaviour, *Chem. Eng. Sci.* 130 (2015) 183-196.

[25] Z. Chang, C. Serra, M. Bouquey, L. Prat and G. Hadziioannou, Co-axial capillaries microfluidic device for synthesizing size- and morphology-controlled polymer core-polymer shell particles, *Lab chip.* 9 (2009) 3007-3011.

[26] K. Potter, B.J. Balcom, T.A. Carpenter, L.D. Hall, The gelation of sodium alginate with calcium ions studied by magnetic resonance imaging (MRI), *Carbohydr. Res.* 257 (1994) 1 117-126.

Graphical abstract

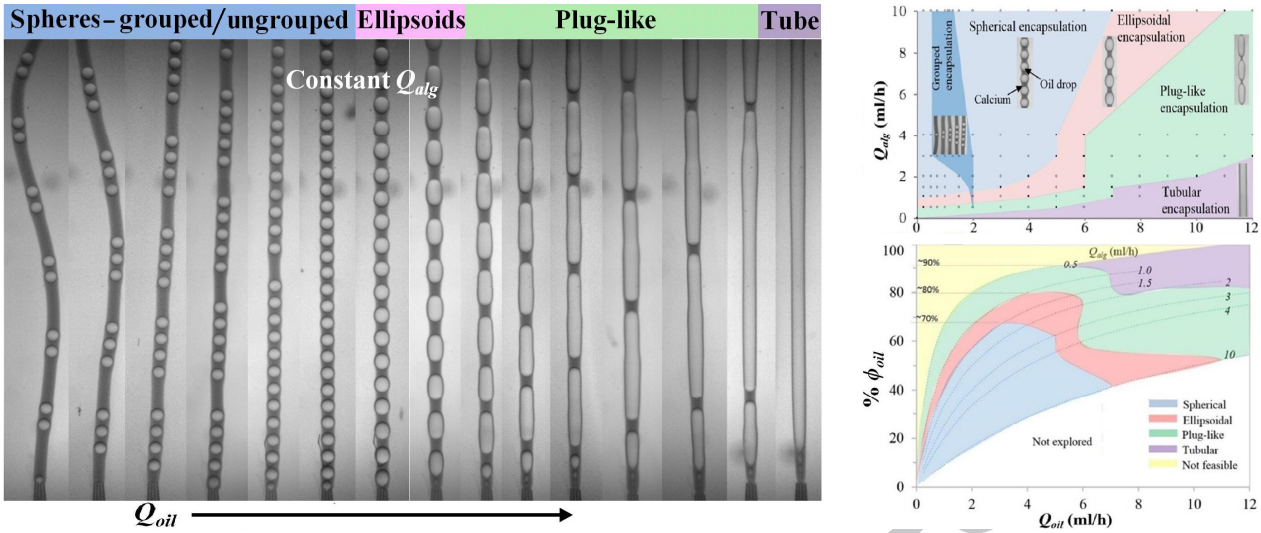

Highlights

- A flexible one-step microfluidic oil encapsulation in alginate fibers is proposed
- Spherical, ellipsoidal, plug-like and tubular encapsulate geometries are achieved
- The relation between oil encapsulation volume and fibers morphology is mapped
- Selective grouping of oil encapsulates is demonstrated
- A force-balance model for predicting size of spherical encapsulates is introduced